

Mathematical Foundations of Data Sciences



Gabriel Peyré
CNRS & DMA
École Normale Supérieure
gabriel.peyre@ens.fr
<https://mathematical-tours.github.io>
www.numerical-tours.com

November 15, 2020

Chapter 4

Linear and Non-linear Approximation

This chapter studies the theory of signal and image approximation, and gives an application to lossy compression. This theoretical analysis is performed for continuous functions $f \in L^2([0, 1]^d)$ for $d = 1, 2$. This analysis is important to studies the performance of compression, denoising, and super-resolution applications.

4.1 Approximation

4.1.1 Approximation in an Ortho-basis

We consider an orthogonal basis $\mathcal{B} = \{\psi_m\}_m$ of $L^2([0, 1]^d)$, with for instance $d = 1$ (signals) or $d = 2$ (images). We recall that the decomposition of a signal in an orthonormal basis

$$f = \sum_{m \in \mathbb{Z}} \langle f, \psi_m \rangle \psi_m$$

gives back the original signal and thus produces no error. Processing algorithms modify the coefficients $\langle f, \psi_m \rangle$ and introduce some error.

The simplest processing computes an approximation by considering only a sub-set $I_M \subset \mathbb{Z}$ of M coefficients and performing the reconstruction from this subset

$$f_M \stackrel{\text{def.}}{=} \sum_{m \in I_M} \langle f, \psi_m \rangle \psi_m, \quad \text{where } M = |I_M|.$$

The reconstructed signal f_M is the orthogonal projection of f onto the space

$$V_M \stackrel{\text{def.}}{=} \text{Span} \{ \psi_m ; m \in I_M \}.$$

Since V_M might depend on f , this projection $f \mapsto f_M$ might be non-linear.

Since the basis is orthogonal, the approximation error is

$$\|f - f_M\|^2 = \sum_{m \notin I_M} |\langle f, \psi_m \rangle|^2.$$

The important question is now to choose the set I_M , which might depend on the signal f itself.

4.1.2 Linear Approximation

Linear approximation is obtained by fixing once for all I_M , and thus using the same set of coefficients for all f . The mapping $f \mapsto f_M$ is a linear orthogonal projection on V_M , and it satisfies

$$(f + g)_M = f_M + g_M$$

For the Fourier basis, one usually selects the low-frequency atoms

$$I_M = \{-M/2 + 1, \dots, M/2\}.$$

For a 1-D wavelet basis, one usually selects the coarse wavelets

$$I_M = \{m = (j, m) ; j \geq j_0\}$$

where j_0 is selected such that $|I_M| = M$.



Figure 4.1: Linear versus non-linear wavelet approximation.

Figure 4.1, center, shows an example of such a linear approximation with wavelets. Linear approximation tends to perform poorly near singularities, because they introduce some blurring.

4.1.3 Non-linear Approximation

A non-linear approximation is obtained by choosing I_M depending on f . In particular, one would like to choose I_M to minimize the approximation error $\|f - f_M\|$. Since the basis is orthogonal, this is achieved by selecting the M largest coefficients in magnitude

$$I_M = \{M \text{ largest coefficients } |\langle f, \psi_m \rangle|\}.$$

This can be equivalently obtained using a thresholding

$$I_M = \{m ; |\langle f, \psi_m \rangle| > T\}$$

where T depends on the number of coefficients M ,

$$M = \# \{m ; |\langle f, \psi_m \rangle| > T\}.$$

Computation of the threshold. There is a bijective 1:1 mapping between T and M obtained by ordering the coefficient magnitudes $|\langle f, \psi_m \rangle|$ by decaying order,

$$T = d_M \quad \text{where} \quad \{d_m\}_{m=0}^{N-1} = \{|\langle f, \psi_m \rangle|\}_0^{N-1} \quad \text{and} \quad d_m \geq d_{m+1}. \quad (4.1)$$

Figure 4.2 shows this mapping between M and T .

The following proposition shows that the decay of the ordered coefficients is linked to the non-linear approximation decay.

Proposition 16. *One has*

$$d_m = O(m^{-\frac{\alpha+1}{2}}) \iff \|f - f_M\|^2 = O(M^{-\alpha}). \quad (4.2)$$

Proof. One has

$$\|f - f_M\|^2 = \sum_{m>M} d_m^2$$

and

$$d_M^2 \leq \frac{2}{M} \sum_{m=M/2+1}^M d_m^2 \leq \frac{2}{M} \sum_{m>M/2} d_m^2 = \frac{2}{M} \|f - f_{M/2}\|^2.$$

□

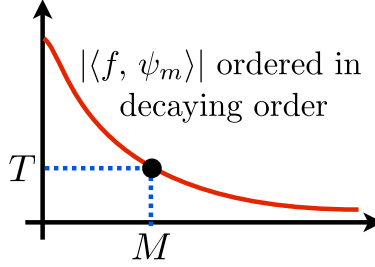


Figure 4.2: Decay of the ordered coefficients and determination of the threshold for non-linear approximation.

Hard thresholding. The non-linear approximation is re-written as

$$f_M = \sum_{|\langle f, \psi_m \rangle| > T} \langle f, \psi_m \rangle \psi_m = \sum_m S_T(\langle f, \psi_m \rangle) \psi_m, \quad (4.3)$$

where

$$S_T(x) = \begin{cases} x & \text{if } |x| > T \\ 0 & \text{if } |x| \leq T \end{cases} \quad (4.4)$$

is the hard thresholding, that is displayed in Figure 4.3.

4.2 Signal and Image Modeling

A signal model is a constraint $f \in \Theta$, where $\Theta \subset L^2([0, 1]^d)$ is a set of signals one is interested in. Figure 4.4 shows different class of models for images, that we describe in the following paragraph.

4.2.1 Uniformly Smooth Signals and Images

Signals with derivatives. The simplest model is made of uniformly smooth signals, that have bounded derivatives

$$\Theta = \{f \in L^2([0, 1]^d) ; \|f\|_{C^\alpha} \leq C\}, \quad (4.5)$$

where $C > 0$ is a fixed constant, and where in 1-D

$$\|f\|_{C^\alpha} \stackrel{\text{def.}}{=} \max_{k \leq \alpha} \left\| \frac{d^k f}{dt^k} \right\|_\infty.$$

This extends to higher dimensional signals by considering partial derivatives along each direction.

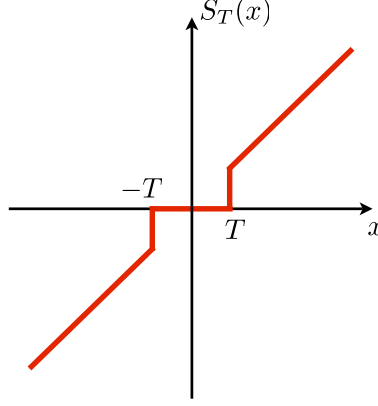


Figure 4.3: Hard thresholding.

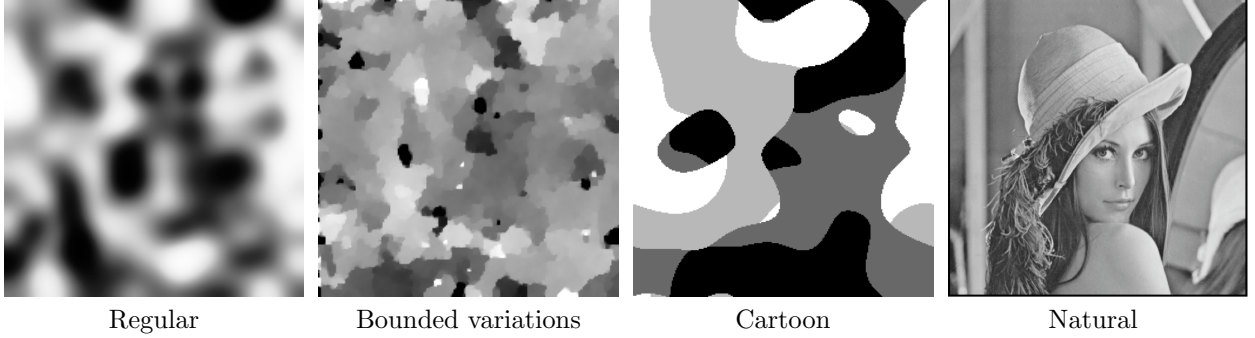


Figure 4.4: Examples of different kinds of image models.

Sobolev smooth signals and images. A smooth C^α signals in (4.5) has derivatives with bounded energy, so that

$$\frac{d^\alpha f}{dt^\alpha}(t) = f^{(\alpha)}(t) \in L^2([0, 1]).$$

Using the fact that

$$\hat{f}_m^{(\alpha)} = (2i\pi m)^\alpha \hat{f}_m$$

where \hat{f} is the Fourier coefficient defined in (2.2), except we are here on \mathbb{R}/\mathbb{Z} in place of $\mathbb{R}/2\pi\mathbb{Z}$,

$$\hat{f}_n \stackrel{\text{def.}}{=} \int_0^1 e^{-2i\pi n x} f(x) dx,$$

one defines a so-called Sobolev functional

$$\|f\|_{\text{Sob}(\alpha)}^2 = \sum_{m \in \mathbb{Z}} |2\pi m|^{2\alpha} |\langle f, e_m \rangle|^2, \quad (4.6)$$

that satisfies $\|f\|_{\text{Sob}(\alpha)} = \|f^{(\alpha)}\|$ for smooth functions. This Sobolev functional is extended to signals that have derivatives in the sense of distribution in $L^2([0, 1])$.

This definition extends to distributions and signals $f \in L^2([0, 1]^d)$ of arbitrary dimension d as

$$\|f\|_{\text{Sob}(\alpha)}^2 = \sum_{m \in \mathbb{Z}^d} (2\pi \|m\|)^{2\alpha} |\langle f, e_m \rangle|^2, \quad (4.7)$$

The C^α -Sobolev model

$$\Theta = \left\{ f \in \ell^2([0, 1]^d) ; \max_{k \leq \alpha} \|f\|_{\text{Sob}(k)}^2 \leq C \right\} \quad (4.8)$$

generalizes the C^α smooth image model (4.5).

Figure 4.5 shows images with an increasing Sobolev norm for $\alpha = 2$.

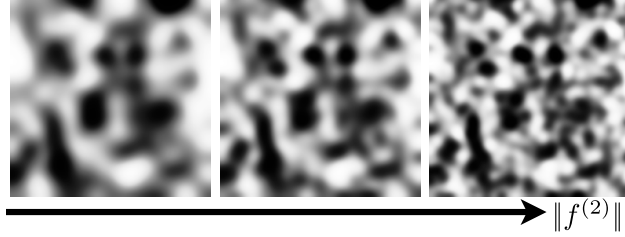


Figure 4.5: Images with increasing Sobolev norm.

4.2.2 Piecewise Regular Signals and Images

Piecewise smooth signals. Piecewise smooth signals in 1-D are functions $f \in L^2([0, 1])$ that are C^α smooth outside a set of less than K pointwise discontinuities

$$\Theta = \{f \in L^2([0, 1]) ; \exists (t_i)_{i=0}^{K-1}, \|f_{(t_i, t_{i+1})}\|_{C^\alpha} \leq C\} \quad (4.9)$$

where $f_{(t_i, t_{i+1})}$ is the restriction of f to the open interval (t_i, t_{i+1}) .

Piecewise smooth images. Piecewise smooth images are 2-D functions $f \in L^2([0, 1]^2)$ that are C^α regular outside a set of less than K curves that have a finite perimeter

$$\Theta = \{f \in L^2([0, 1]^2) ; \exists \Gamma = (\gamma_i)_{i=0}^{K-1}, \|f\|_{C^\alpha(\Gamma^c)} \leq C_1 \quad \text{and} \quad |\gamma_i| \leq C_2\} \quad (4.10)$$

where $|\gamma_i|$ is the length of the curve γ_i and where $\|f\|_{C^\alpha(\Gamma^c)}$ is the maximum norm of the derivatives of f outside the set of curves Γ .

Segmentation methods such as the one proposed by Mumford and Shah [18] implicitly assume such a piecewise smooth image model.

4.2.3 Bounded Variation Signals and Images

Signals with edges are obtained by considering functions with bounded variations

$$\Theta = \{f \in L^2(\mathbb{R}^d) ; \|f\|_\infty \leq C_1 \quad \text{and} \quad \|f\|_{\text{TV}} \leq C_2\}. \quad (4.11)$$

For $d = 1$ and $d = 2$, this model generalizes the model of piecewise smooth signals (4.9) and images (4.10).

The total variation of a smooth function is

$$\int \|\nabla f(x)\| dx$$

where

$$\nabla f(x) = \left(\frac{\partial f}{\partial x_i} \right)_{i=0}^{d-1} \in \mathbb{R}^d$$

is the gradient vector at x . The total variation is extended to discontinuous images, that might for instance exhibit jumps across singular curves (the edges of the image). In particular, the total variation of a piecewise smooth image is the sum of the lengths of its level sets

$$\|f\|_{\text{TV}} = \int_{-\infty}^{\infty} |\mathcal{L}_t(f)| dt < +\infty \quad \text{where} \quad \mathcal{L}_t(f) = \{x; f(x) = t\}, \quad (4.12)$$

and where $|\mathcal{L}_t(f)|$ is the length of $\mathcal{L}_t(f)$. For a set $\Omega \subset \mathbb{R}^2$ with finite perimeter $|\partial\Omega|$, then

$$\|1_\Omega\|_{\text{TV}} = |\partial\Omega|.$$

The model of bounded variation was introduced in image processing by Rudin, Osher and Fatemi [22].

4.2.4 Cartoon Images

The bounded variation image model (4.11) does not constrain the smoothness of the level set curves $\mathcal{L}_t(f)$. Geometrical images have smooth contour curves, which should be taken into account to improve the result of processing methods.

The model of C^α cartoon images is composed of 2-D functions that are C^α regular outside a set of less than K regular edge curves γ_i

$$\Theta = \{f \in L^2([0, 1]^2); \exists \Gamma = (\gamma_i)_{i=0}^{K-1}, \|f\|_{C^\alpha(\Gamma^c)} \leq C_1 \quad \text{and} \quad \|\gamma_i\|_{C^\alpha} \leq C_2\} \quad (4.13)$$

where each γ_i is a arc-length parameterization of the curve $\gamma_i : [0, A] \mapsto [0, 1]^2$. Figure 4.6 shows cartoon images with increasing total variation $\|f\|_{\text{TV}}$.



Figure 4.6: Cartoon image with increasing total variation.

Typical images might also be slightly blurred by optical diffraction, so that one might consider a blurred cartoon image model

$$\tilde{\Theta} = \left\{ \tilde{f} = f \star h \in L^2([0, 1]^2); f \in \Theta \quad \text{and} \quad h \in \mathcal{H} \right\} \quad (4.14)$$

where Θ is the model of sharp (unblurred) images (4.13) and \mathcal{H} is a set of constraints on the blurring kernel, for instance $h \geq 0$ should be smooth, localized in space and frequency. This unknown blurring makes difficult brute force approaches that detects the edges location Γ and then process the regular parts in $[0, 1]^2 \setminus \Gamma$.

Figure 4.7 shows examples of images in Θ and $\tilde{\Theta}$.

4.3 Efficient approximation

4.3.1 Decay of Approximation Error

To perform an efficient processing of signals or images in Θ , the goal is to design an orthogonal basis such that the non-linear approximation error $\|f - f_M\|$ decays as fast as possible to 0 when M increases.

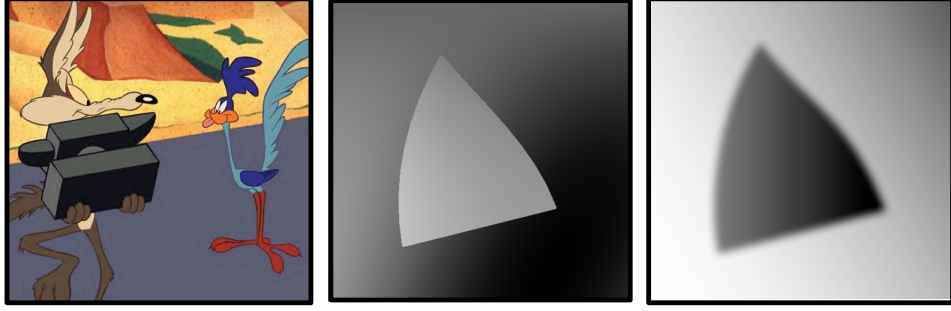


Figure 4.7: Examples of cartoon images: sharp discontinuities (left and center) and smooth discontinuities (right).

Polynomial error decay. This error decay measured using a power law

$$\forall f \in \Theta, \forall M, \quad \|f - f_M\|^2 \leq C_f M^{-\alpha} \quad (4.15)$$

where α is independent of f and should be as large as possible. The parameter α depends on the basis and on Θ . It is a class-complexity parameter that describes the overall complexity of signals in Θ with respect to the orthogonal basis one considers for approximation. The parameter C_f depends on f and describes the complexity of the signal f within its class Θ .

Relevance for compression, denoising and inverse problems. Monitoring the decay of approximation error is not only interesting from a mathematical point of view. Section 5.1 shows that the compression error is close to the non-linear approximation error. Bases that are efficient for approximation are thus also efficient for compression.

Chapter ?? shows that a similar conclusion holds for non-linear denoising with thresholding. Efficient denoisers are obtained by performing a non-linear approximation of the noisy image in a well chosen basis. The average denoising error with respect to a random noise is closely related to the approximation error.

Chapter ?? shows that ill-posed inverse problems such as super-resolution of missing information can be solved by taking advantage of the compressibility of the signal or the image in a well chosen basis. A basis that is efficient for approximation of the high resolution signal is needed to recover efficiently missing information. The performance of these schemes is difficult to analyze, and the basis atoms must also be far enough from the kernel of the operator that removes information.

Comparison of signals. For a fixed basis (for instance wavelets), the decay of $\|f - f_M\|$ allows one to compare the complexity of different images. Figure 4.9 shows that natural images with complicated geometric structures and textures are more difficult to approximate using wavelets.

Since the approximation error often decays in a power-low fashion (4.15), the curves are displayed in a log-log plot, so that

$$\log(\|f - f_M\|^2) = \text{cst} - \alpha \log(M)$$

and hence one should expect an affine curve with slope $-\alpha$. Due to discretization issue, this is only the case for value of $M \ll N$, since the error quickly drops to zero for $M \approx N$.

4.3.2 Comparison of bases.

For a given image f , one can compare different ortho-bases using the decay of $\|f - f_M\|$. Figure 4.11 shows the efficiency of several bases to approximate a fixed natural image with contours and textures. The Fourier basis described in Section ?? is highly inefficient because of periodic boundary artifact and the global

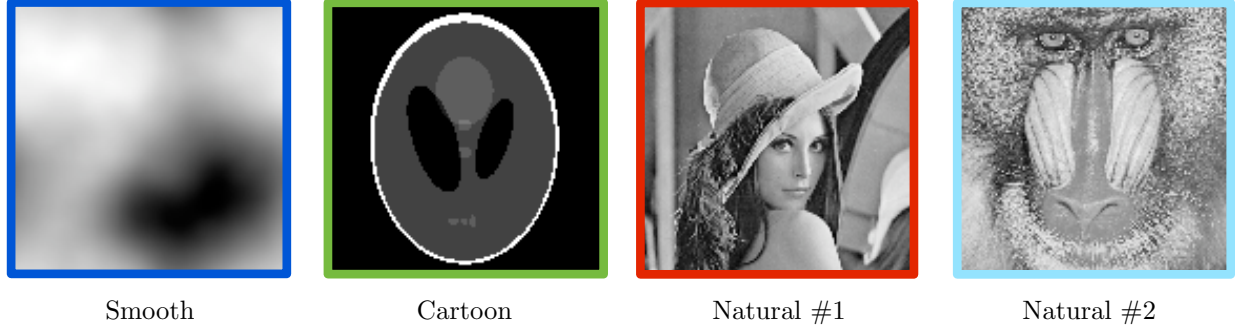


Figure 4.8: Several different test images.

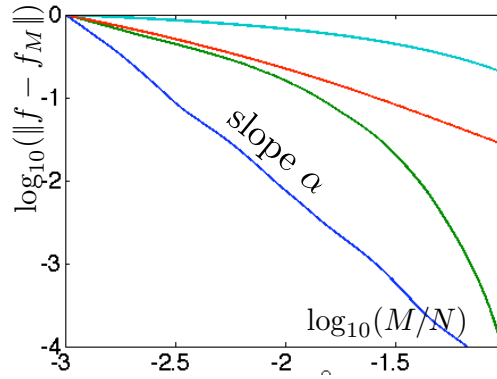


Figure 4.9: Comparison of approximation error decay in wavelets for different images shown in Figure 4.8.

support of its atoms that fail to capture contours. The cosine basis uses symmetric boundary conditions and thus removes the boundary artifacts, but it is still not able to resolve efficiently localized features. The local DCT basis corresponds to the union of local cosine bases defined on small square patches. It is more efficient since its atoms have a local support. However, it gives bad approximation for a small number M of kept coefficients, because of blocking artifacts. The isotropic wavelet basis detailed in Section ?? gives the best approximation results because it is both composed of localized atoms and does not have a block structure but rather a multiresolution structure.

Figure 4.12 summarizes the different type of approximation decays for various class of data, which are detailed in the following section.

4.4 Fourier Linear Approximation of Smooth Functions

The smooth signal and image model (4.5) assumed that the analog function have bounded α continuous derivatives. A function f with a large α has more smoothness, and is thus simpler to approximate. Figure 4.5 shows images with increasing smoothness.

4.4.1 1-D Fourier Approximation

A 1-D signal $f \in L^2([0, 1])$ is associated to a 1-periodic function $f(t + 1) = f(t)$ defined for $t \in \mathbb{R}$.



Figure 4.10: Comparison of approximation errors for different bases using the same number $M = N/50$ of coefficients.

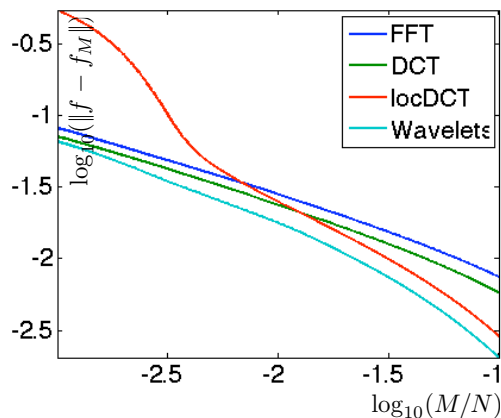


Figure 4.11: Comparison of approximation error decay for different bases.

Low pass approximation. We consider a linear Fourier approximation, that only retains low frequencies

$$f_M^{\text{lin}} = \sum_{m=-M/2}^{M/2} \langle f, e_m \rangle e_m$$

where we use the 1-D Fourier atoms

$$\forall n \in \mathbb{Z}, \quad e_m(t) \stackrel{\text{def.}}{=} e^{2i\pi mt}.$$

We note that f_M actually requires $M + 1$ Fourier atoms.

Figure 4.13 shows examples of such linear approximation for an increasing value of M . Since the original function f is singular (no derivative), this produces a large error and one observe ringing artifacts near singularities.

This low pass approximation corresponds to a filtering, since

$$f_M = \sum_{m=-M/2}^{M/2} \langle f, e_m \rangle e_m = f \star h_M \quad \text{where} \quad \hat{h}_M \stackrel{\text{def.}}{=} 1_{[-M/2, M/2]}.$$

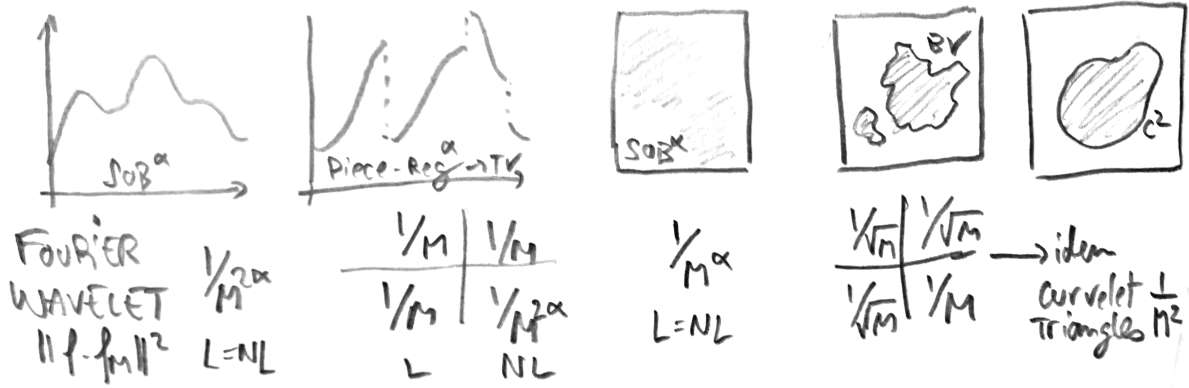


Figure 4.12: Summary of linear and non-linear approximation rates $\|f - f_M\|^2$ for different classes of 1-D signals and images.

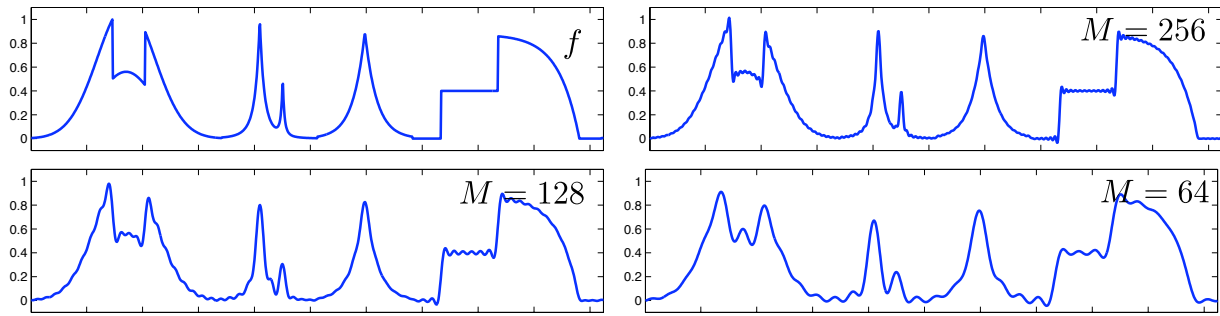


Figure 4.13: Fourier approximation of a signal.

Here, h_M is the so-called Dirichlet kernel (see also the chapter on Fourier).

The following proposition shows that this approximation decays fast for C^α signals.

Proposition 17. *One has for $f \in C^\alpha(\mathbb{R}/\mathbb{Z})$*

$$\|f - f_M^{\text{lin}}\|^2 = O(M^{-2\alpha+1}).$$

Proof. Using integration by part, one shows that for a C^α function f in the smooth signal model (4.5), $\mathcal{F}(f^{(\ell)})_m = (2im\pi)^\ell \hat{f}_m$, so that one has using Cauchy-Schwartz

$$|\langle f, e_m \rangle| \leq |2\pi m|^{-\alpha} \|f^{(\alpha)}\|_2.$$

This implies

$$\|f - f_M^{\text{lin}}\|^2 = \sum_{|m| > M/2} |\langle f, e_m \rangle|^2 \leq \|f^{(\alpha)}\|_2^2 \sum_{|m| > M/2} |2\pi m|^{-2\alpha} = O(M^{-2\alpha+1}).$$

□

We show next that a slightly modified proof gives a better decay (assuming $f^{(\alpha)}$ is in $L^2(\mathbb{R}/\mathbb{Z})$) and that this conclusion is valid for a larger class of Sobolev functions.

Proposition 18. For signal f in the Sobolev model (4.8), i.e. $f^{(\alpha)} \in L^2(\mathbb{R})$, one has

$$\|f - f_M^{\text{lin}}\|^2 \leq C \|f^{(\alpha)}\|^2 M^{-2\alpha}. \quad (4.16)$$

Proof. One has

$$\|f^{(\alpha)}\|^2 = \sum_m |2\pi m|^{2\alpha} |\langle f, e_m \rangle|^2 \geq \sum_{|m| > M/2} |2\pi m|^{2\alpha} |\langle f, e_m \rangle|^2 \quad (4.17)$$

$$\geq (\pi M)^{2\alpha} \sum_{m > M/2} |\langle f, e_m \rangle|^2 \geq (\pi M)^{2\alpha} \|f - f_M^{\text{lin}}\|^2. \quad (4.18)$$

□

One can also show that this asymptotic error decay is optimal, and that the non-linear approximation error in Fourier also decays like $O(M^{-2\alpha})$.

For a signal in the piecewise smooth model (4.9), such as the one shown in Figure 4.13, one only has a slow decay of the linear and non-linear approximation error

$$\|f - f_M\|^2 \leq C_f M^{-1} \quad (4.19)$$

and Fourier atoms are not anymore optimal for approximation. A typical example is $f = 1_{[a, b]}$ the indicator of a step, for which $|\hat{f}_m| \sim 1/m$, and thus $\|f - f_M\|^2 \sim \sum_{|m| > M} 1/|m|^2 \sim 1/M$ for both linear and non-linear approximations.

4.4.2 Sobolev Images

This analysis carries over to images and higher dimensional datasets by considering a Sobolev functional (4.7) for $d > 1$.

The linear and non-linear approximation of an α -regular Sobolev image then satisfy

$$\|f - f_M\|^2 \leq C \|f^\alpha\|^2 M^{-\alpha}.$$

For d -dimensional data $f : [0, 1]^d \rightarrow \mathbb{R}$, one would have an error decay of $O(M^{-2\alpha/d})$.

For an image in the piecewise smooth model (4.10), the linear and non-linear error decays are slow,

$$\|f - f_M\|^2 \leq C_f M^{-1/2}, \quad (4.20)$$

and Fourier atoms are not anymore optimal for approximation.

4.5 Wavelet Approximation of Piecewise Smooth Functions

Wavelet approximation improves significantly over Fourier approximation to capture singularities. This is due to the localized support of wavelets.

4.5.1 Decay of Wavelet Coefficients

To efficiently approximate regular parts of signals and images, one uses wavelet with a large enough number p of vanishing moments

$$\forall k < p, \int \psi(x) x^k dx = 0.$$

This number p should be larger than the regularity α of the signal outside singularities (for instance jumps or kinks).

To quantify the approximation error decay for piecewise smooth signals (4.9) and images (4.10), one needs to treat differently wavelets that are in regular and singular areas. Figure 4.15 shows for a signal and an image the localization of singular and regular parts.



Figure 4.14: Linear (top row) and non-linear (bottom row) Fourier approximation.

Proposition 19. *If f is C^α on $\text{supp}(\psi_{j,n})$, with $p \geq \alpha$, one has*

$$|\langle f, \psi_{j,n} \rangle| \leq C_f \|\psi\|_1 2^{j(\alpha+d/2)}. \quad (4.21)$$

In general, one always has for bounded f

$$|\langle f, \psi_{j,n} \rangle| \leq \|f\|_\infty \|\psi\|_1 2^{j\frac{d}{2}}.$$

Proof. If f is C^α on $\text{supp}(\psi_{j,n})$, with $p \geq \alpha$, then one can perform a Taylor expansion of f around the point $2^j n$

$$f(x) = P(x - 2^j n) + R(x - 2^j n) = P(2^j t) + R(2^j t)$$

where $\deg(P) < \alpha$ and

$$|R(x)| \leq C_f \|x\|^\alpha.$$

One then bounds the wavelet coefficient

$$\langle f, \psi_{j,n} \rangle = \frac{1}{2^{j\frac{d}{2}}} \int f(x) \psi\left(\frac{x - 2^j n}{2^j}\right) dx = 2^{j\frac{d}{2}} \int R(2^j t) \psi(t) dt$$

where we have performed the change of variable $t = \frac{x - 2^j n}{2^j}$. This shows that (4.21) holds. Property (19) is straightforward. \square

4.5.2 1-D Piecewise Smooth Approximation

For 1-D signal in the piecewise regular model (4.9), large wavelets coefficients $\langle f, \psi_{j,n} \rangle$ are clustered around the singularities of the signal. We call $\mathcal{S} \subset [0, 1]$ the finite set of singular points.

Theorem 5. *f is in the piecewise smooth signal model (4.9), the non-linear approximation error in wavelet obeys*

$$\|f - f_M\|^2 = O(M^{-2\alpha}). \quad (4.22)$$

Proof. The proof is split in several parts.

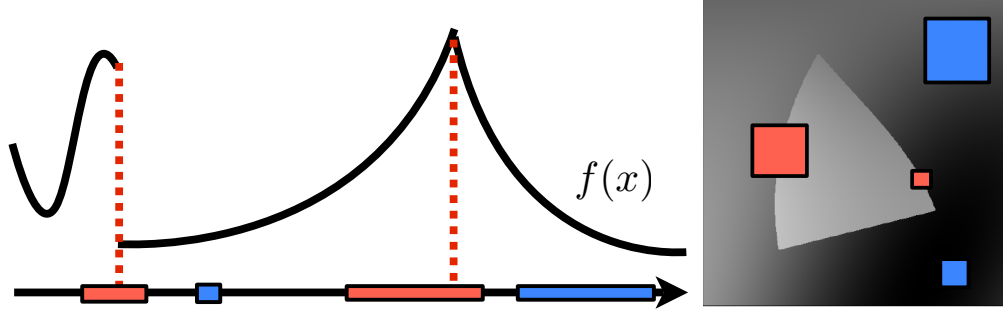


Figure 4.15: Singular par of signals (left) and image (right).

Step 1. Coefficient segmentation. The singular support at scale 2^j is the set of coefficients corresponding to wavelets that are crossing a singularity

$$\mathcal{C}_j = \{n ; \text{supp}(\psi_{j,n}) \cap \mathcal{S} \neq \emptyset\} \quad (4.23)$$

It has a constant size because of the dyadic translation of wavelets

$$|\mathcal{C}_j| \leq K|\mathcal{S}| = \text{constant}.$$

Using (4.21) for $d = 1$, the decay of regular coefficients is bounded as

$$\forall n \in \mathcal{C}_j^c, \quad |\langle f, \psi_{j,n} \rangle| \leq C2^{j(\alpha+1/2)}.$$

Using (19) for $d = 1$, the decay of singular coefficients is bounded as

$$\forall n \in \mathcal{C}_j, \quad |\langle f, \psi_{j,n} \rangle| \leq C2^{j/2}.$$

Once a fixed threshold T is fixed to compute the non-linear approximation, one defines cut-off scales for regular and singular coefficients that depend on T

$$2^{j_1} = (T/C)^{\frac{1}{\alpha+1/2}} \quad \text{and} \quad 2^{j_2} = (T/C)^2.$$

Figure 4.16 shows a schematic segmentation of the set of wavelet coefficients into regular and singular parts, and also using the cut-off scales.

Step 2. Counting the error. These cut-off scales allow us to define a hand-crafted approximation signal

$$\tilde{f}_M = \sum_{j \geq j_2} \sum_{n \in \mathcal{C}_j} \langle f, \psi_{j,n} \rangle \psi_{j,n} + \sum_{j \geq j_1} \sum_{n \in \mathcal{C}_j^c} \langle f, \psi_{j,n} \rangle \psi_{j,n}. \quad (4.24)$$

The approximation error generated by this M -term approximation \tilde{f}_M is larger than the best M -term approximation error, and hence

$$\|f - f_M\|^2 \leq \|f - \tilde{f}_M\|^2 \leq \sum_{j < j_2, n \in \mathcal{C}_j} |\langle f, \psi_{j,n} \rangle|^2 + \sum_{j < j_1, n \in \mathcal{C}_j^c} |\langle f, \psi_{j,n} \rangle|^2 \quad (4.25)$$

$$\leq \sum_{j < j_2} (K|\mathcal{S}|) \times C^2 2^j + \sum_{j < j_1} 2^{-j} \times C^2 2^{j(2\alpha+1)} \quad (4.26)$$

$$= O(2^{j_2} + 2^{2\alpha j_1}) = O(T^2 + T^{\frac{2\alpha}{\alpha+1/2}}) = O(T^{\frac{2\alpha}{\alpha+1/2}}). \quad (4.27)$$

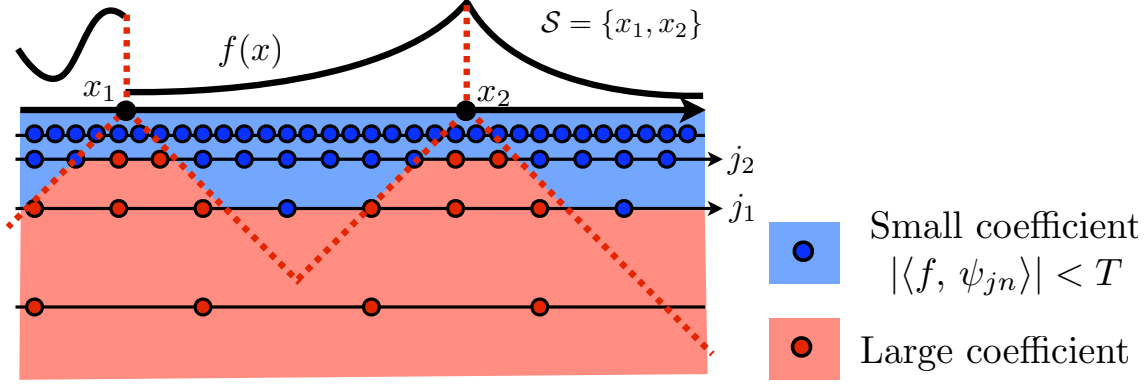


Figure 4.16: Segmentation of the wavelet coefficients into regular and singular parts.

Step 3. Counting the number of measurements. The number of coefficients needed to build the approximating signal \tilde{f}_M is

$$M \leq \sum_{j \geq j_2} |\mathcal{C}_j| + \sum_{j \geq j_1} |\mathcal{C}_j^c| \leq \sum_{j \geq j_2} K|\mathcal{S}| + \sum_{j \geq j_1} 2^{-j} \quad (4.28)$$

$$= O(|\log(T)| + T^{\frac{-1}{\alpha+1/2}}) = O(T^{\frac{-1}{\alpha+1/2}}). \quad (4.29)$$

Step 3. Putting everything together. Putting equations (4.25) and (4.28) together gives the desired result. \square

This theorem improves significantly over the $O(M^{-1})$ decay of Fourier approximation (4.19). Furthermore, this decay is the same as the error decay of uniformly smooth signal (4.16). In 1-D, wavelet approximations do not “see” the singularities. The error decay (4.22) can be shown to be asymptotically optimal.

Figure 4.17 shows examples of wavelet approximation of singular signals.

4.5.3 2-D Piecewise Smooth Approximation

We now give the equivalent of Theorem 5 but for 2-D functions.

Theorem 6. *f is in the piecewise smooth signal model (4.10), the non-linear approximation error in wavelet obeys*

$$\|f - f_M\|^2 = O(M^{-1}). \quad (4.30)$$

Proof. For an image in the piecewise smooth model (4.10), we define the singular support \mathcal{C}_j as in (4.23). The major difference with the 1-D setting, is that for 2-D images, the size of the singular support grows when the scale 2^j goes to zero

$$|\mathcal{C}_j^\omega| \leq 2^{-j} K|\mathcal{S}|,$$

where $|\mathcal{S}|$ is the perimeter of the singular curves \mathcal{S} , and $\omega \in \{V, H, D\}$ is the wavelet orientation. Using (4.21) for $d = 2$, the decay of regular coefficients is bounded as

$$\forall n \in (\mathcal{C}_j^\omega)^c, \quad |\langle f, \psi_{j,n}^\omega \rangle| \leq C 2^{j(\alpha+1)}.$$

Using (19) for $d = 2$, the decay of singular coefficients is bounded as

$$\forall n \in \mathcal{C}_j^\omega, \quad |\langle f, \psi_{j,n}^\omega \rangle| \leq C 2^j.$$

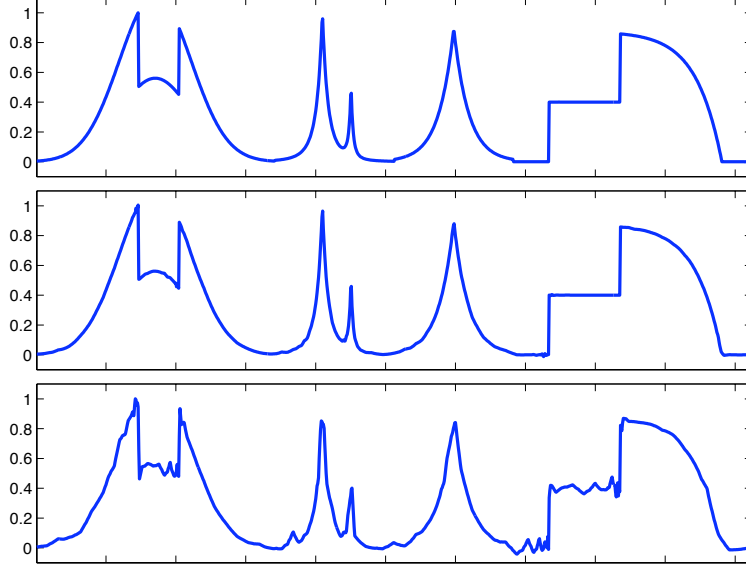


Figure 4.17: 1-D wavelet approximation.

After fixing T , the cut-off scales are defined as

$$2^{j_1} = (T/C)^{\frac{1}{\alpha+1}} \quad \text{and} \quad 2^{j_2} = T/C.$$

We define similarly to (4.24) a hand-made approximation. Similarly to (4.25), we bound the approximation error as

$$\|f - f_M\|^2 \leq \|f - \tilde{f}_M\|^2 = O(2^{j_2} + 2^{2\alpha j_1}) = O(T + T^{\frac{2\alpha}{\alpha+1}}) = O(T)$$

and the number of coefficients as

$$M = O(T^{-1} + T^{\frac{-1}{\alpha+1}}) = O(T^{-1}).$$

This leads to the announced decay of the non-linear wavelet approximation error. \square

This improves significantly over the $O(M^{-1/2})$ decay of Fourier approximation (4.20). This result is however deceiving, since it does not take advantage of the C^α regularity of the image outside the edge curves.

This error decay is still valid for the more general model of images with bounded variations (4.11). One can show that wavelets are asymptotically optimal to approximate images with bounded variations.

Figure 4.18 shows wavelet approximations of a bounded variation image.

4.6 Cartoon Images Approximation

The square support of wavelet makes them inefficient to approximate geometric images (4.13), whose edges are more regular than the level set of bounded variation images (4.11), which are only assumed to be of finite length.

4.6.1 Wavelet Approximation of Cartoon Images

Result (4.30) shows that wavelet approximation of images in the cartoon models (4.13) decays at least like $O(M^{-1})$. One can show that simple cartoon images like $f = 1_\Omega$ where Ω is a disk reach this low decay



Figure 4.18: 2-D wavelet approximation.

speed. This is because the square support of wavelets forbid them to take advantage of the regularity of edge curves. The approximation error for the smoothed cartoon model (4.14) is also slow if the width of the blurring kernel is small with respect to the number M of coefficients.

Figure 4.19 shows that many large coefficients are located near edge curves, and retaining only a small number leads to a bad approximation with visually unpleasant artifacts.

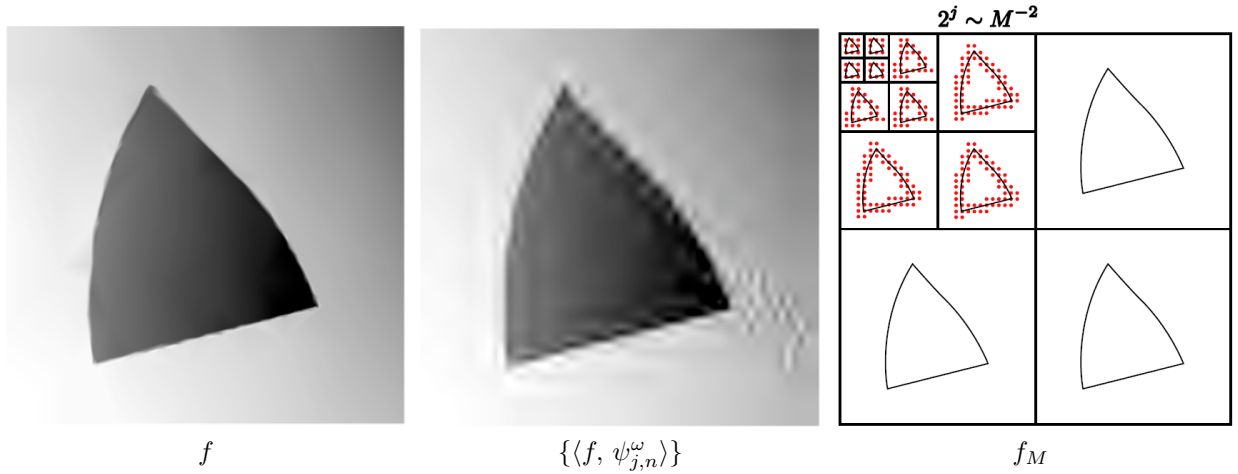


Figure 4.19: Wavelet approximation of a cartoon image.

4.6.2 Finite Element Approximation

To improve over the wavelet approximation, one can design an adapted triangulation that is highly anisotropic near edges. Figure 4.20 shows an example of such a triangulation.

A triangulation is obtained by sampling M points over the image domain $[0, 1]^2$ and then connecting them using triangles. One then defines a piecewise linear interpolation \tilde{f}_M over these triangles.

As shown in Figure 4.21, an efficient approximation of a C^2 -cartoon image (4.13) for $\alpha = 2$ is obtained by seeding $\approx M/2$ approximately equilateral triangles of width $\approx M^{-1/2}$ in the areas where the image is regular. Near the edges, using the C^2 regularity of the singular curve, one can seed $\approx M/2$ anisotropic triangles of length M^{-1} and width $\approx M^{-1/2}$. One can show that such an adaptive triangulation leads to an

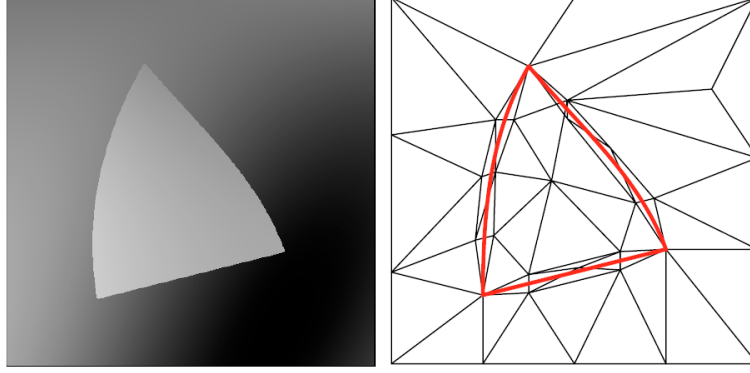


Figure 4.20: Left: cartoon image, right: adaptive triangulation.

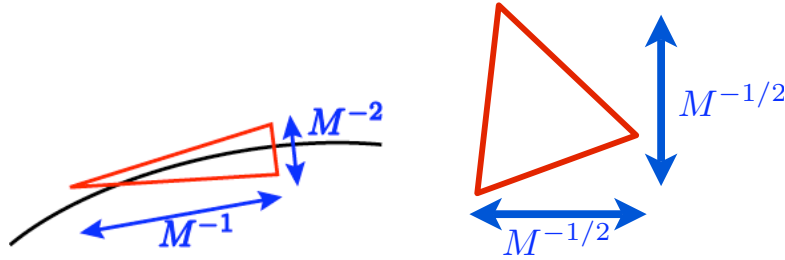


Figure 4.21: Aspect ratio of triangle away from edges (left) and near an edge (right).

approximation error

$$\|f - f_M\|^2 = O(M^{-2}), \quad (4.31)$$

which improves over the wavelet approximation error decay (4.30).

This scheme is however difficult to implement in practice, since the edge curves are not known and difficult to find. This is in particular the case for smooth cartoon images when the smoothing kernel h is unknown.

There is currently no known algorithm that can automatically produces the error decay (4.31). One thus has to use heuristics and greedy algorithm to find the location of the sampling points and computes the triangles. Figure (4.22) shows an example of compression using such a greedy seeding algorithm, that works well in practice.

4.6.3 Curvelets Approximation

Instead of using an adaptive approximation scheme such as finite elements, one can replace the wavelet basis by a set of oriented anisotropic atoms. The curvelet frame was proposed by Candès and Donoho for this purpose [4].

Curvelets. The curvelet construction starts from a curvelet function c that is oriented along the horizontal direction, and perform stretching

$$c_{2^j}(x_1, x_2) \approx 2^{-3j/4} c(2^{-j/2} x_1, 2^{-j} x_2),$$



Figure 4.22: Comparison of adaptive triangulation and JPEG-2000, with the same number of bits.

translation and rotation

$$c_{2^j, u}^\theta(x_1, x_2) = c_{2^j}(R_\theta(x - u))$$

where R_θ is the rotation of angle θ .

The atoms $c_{2^j, u}^\theta$ is located near u , with an orientation θ , and has an aspect ratio “width \approx length²”, which is the same aspect used to build an adaptive finite element approximation. This aspect ratio is essential to capture the anisotropic regularity near edges for images in the cartoon model (4.13) for $\alpha = 2$.

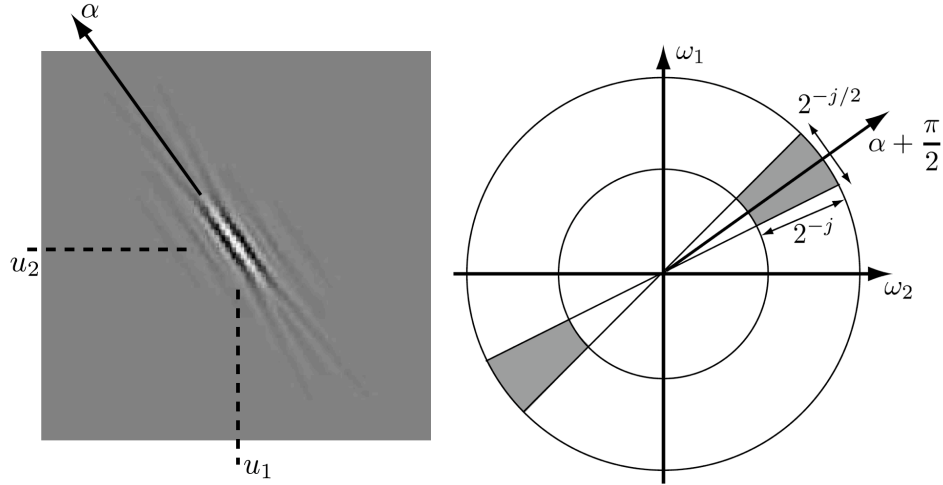


Figure 4.23: Left: a curvelet c_m , right: its Fourier transform localization.

Figure 4.24 shows the spacial and frequency localization of curvelets.

Parameter discretization. To build an image representation, one need to sample the u and θ parameter. To maintain a stable representation, the sub-sampling of the angles depends on the scale

$$\forall 0 \leq k < 2^{-\lceil j/2 \rceil + 2}, \quad \theta_k^{(j)} = k\pi 2^{\lceil j/2 \rceil - 1}$$

and the spacial grid depends on the scale and on the angles

$$\forall m = (m_1, m_2) \in \mathbb{Z}^2, \quad u_m^{(j,\theta)} = R_\theta(2^{j/2}m_1, 2^j m_2).$$

Figure 4.24 shows this sampling pattern.

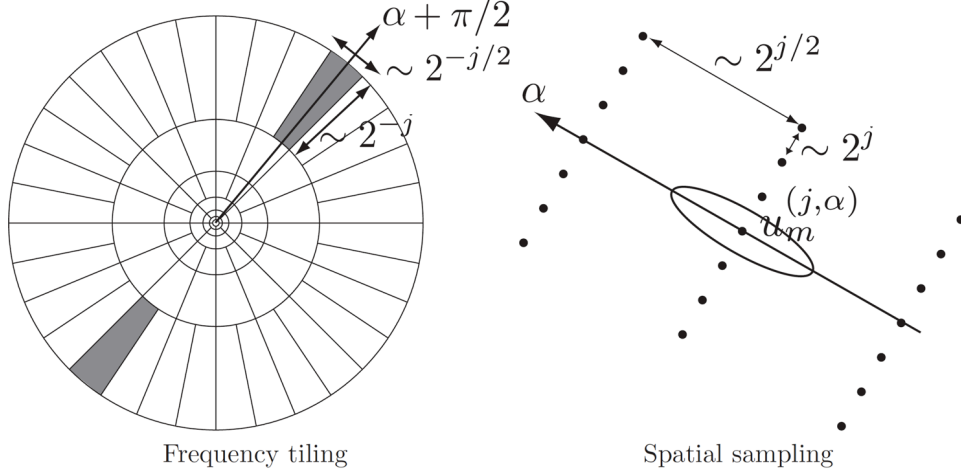


Figure 4.24: Sampling pattern for the curvelet positions.

Curvelet tight frame. This sampling leads to a stable redundant family

$$C_{j,m,k}(x) = c_{2^j, u}^\theta(x) \quad \text{where} \quad \theta = \theta_k^{(j)} \quad \text{and} \quad u = u_m^{(j,\theta)},$$

that obeys a conservation of energy

$$\|f\|^2 = \sum_{j \in \mathbb{Z}} \sum_{k=0}^{2^{-\lceil j/2 \rceil} + 2} \sum_{m \in \mathbb{Z}^2} |\langle f, C_{j,m,k} \rangle|^2$$

and a reconstruction formula

$$f = \sum_{j \in \mathbb{Z}} \sum_{k=0}^{2^{-\lceil j/2 \rceil} + 2} \sum_{m \in \mathbb{Z}^2} \langle f, C_{j,m,k} \rangle C_{j,m,k}$$

that extends the properties of orthogonal basis (tight frame), although the representation is redundant (the atoms are not orthogonal).

A numerical implementation of this tight frame also defines a discrete tight frame for image of N pixels, that is made of $\approx 5N$ atoms [5].

Curvelet approximation. A non-linear M -term approximation in curvelets is defined as

$$f_M = \sum_{|\langle f, C_{j,m,k} \rangle| > T} \langle f, C_{j,m,k} \rangle C_{j,m,k}$$

where T is a threshold that depends on M . One should note that f_M is not necessarily the best M -term curvelet approximation since the curvelet frame is not orthogonal.

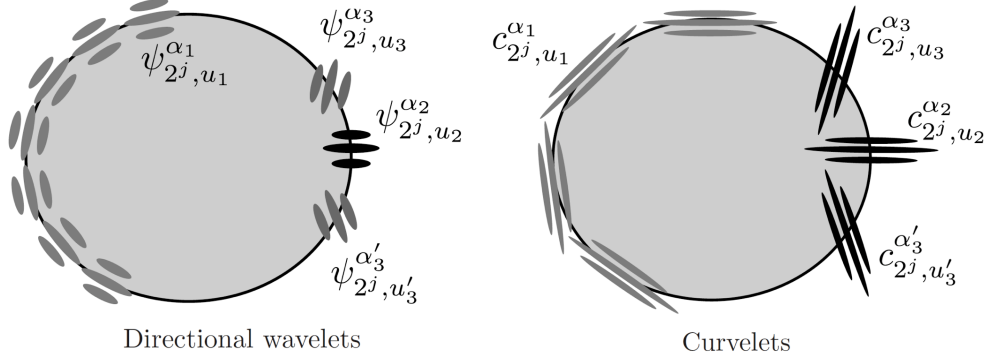


Figure 4.25: Comparison of the principle of wavelets (left) and curvelet (right) approximations of a cartoon image.

For position $u_m^{(j, \theta)}$ that are far away from an edges, the vanishing moments of the curvelets create a small coefficient $\langle f, C_{j, m, k} \rangle$. If $u_m^{(j, \theta)}$ is close to an edge curve whose tangent has direction $\tilde{\theta}$, then the coefficient $\langle f, C_{j, m, k} \rangle$ decays very fast to zero when $|\theta - \tilde{\theta}|$ increases. Figure 4.25 shows the principle of this curvelet approximation, and compares it with directional wavelets that have a square support.

Using these two properties together with the sparse sampling of the curvelet in space and orientation leads to the following approximation error decay

$$\|f - f_M\|^2 = O(\log^3(M)M^{-2})$$

for image in the cartoon model (4.13) for $\alpha = 2$. This is close to the decay of adaptive triangulations (4.31), but this time one computes f_M with a fast $O(N \log(N))$ algorithm for an image of N pixels.

In practice, the redundancy of the curvelet frame makes it not suitable for image compression. Its efficiency is however useful for denoising purpose, where it can improve over wavelet to denoise geometric images and textures, see Figure 4.26. The result is obtained by using a thresholding denoiser as detailed in Section 6.3.1.

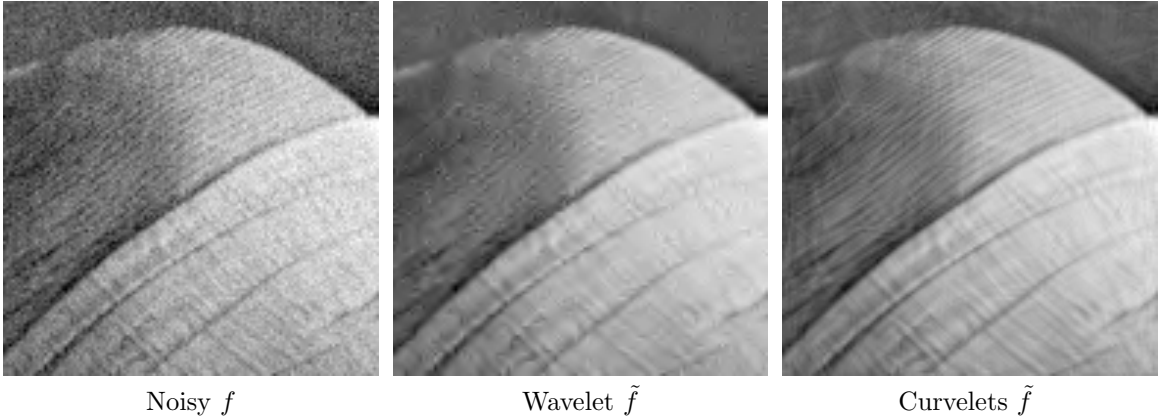


Figure 4.26: Comparison of wavelets (translation invariant) and curvelet denoising.

Bibliography

- [1] Amir Beck. *Introduction to Nonlinear Optimization: Theory, Algorithms, and Applications with MATLAB*. SIAM, 2014.
- [2] Stephen Boyd, Neal Parikh, Eric Chu, Borja Peleato, and Jonathan Eckstein. Distributed optimization and statistical learning via the alternating direction method of multipliers. *Foundations and Trends® in Machine Learning*, 3(1):1–122, 2011.
- [3] Stephen Boyd and Lieven Vandenberghe. *Convex optimization*. Cambridge university press, 2004.
- [4] E. Candès and D. Donoho. New tight frames of curvelets and optimal representations of objects with piecewise C^2 singularities. *Commun. on Pure and Appl. Math.*, 57(2):219–266, 2004.
- [5] E. J. Candès, L. Demanet, D. L. Donoho, and L. Ying. Fast discrete curvelet transforms. *SIAM Multiscale Modeling and Simulation*, 5:861–899, 2005.
- [6] A. Chambolle. An algorithm for total variation minimization and applications. *J. Math. Imaging Vis.*, 20:89–97, 2004.
- [7] Antonin Chambolle, Vicent Caselles, Daniel Cremers, Matteo Novaga, and Thomas Pock. An introduction to total variation for image analysis. *Theoretical foundations and numerical methods for sparse recovery*, 9(263-340):227, 2010.
- [8] Antonin Chambolle and Thomas Pock. An introduction to continuous optimization for imaging. *Acta Numerica*, 25:161–319, 2016.
- [9] S.S. Chen, D.L. Donoho, and M.A. Saunders. Atomic decomposition by basis pursuit. *SIAM Journal on Scientific Computing*, 20(1):33–61, 1999.
- [10] Philippe G Ciarlet. Introduction à l’analyse numérique matricielle et à l’optimisation. 1982.
- [11] P. L. Combettes and V. R. Wajs. Signal recovery by proximal forward-backward splitting. *SIAM Multiscale Modeling and Simulation*, 4(4), 2005.
- [12] I. Daubechies, M. Defrise, and C. De Mol. An iterative thresholding algorithm for linear inverse problems with a sparsity constraint. *Commun. on Pure and Appl. Math.*, 57:1413–1541, 2004.
- [13] D. Donoho and I. Johnstone. Ideal spatial adaptation via wavelet shrinkage. *Biometrika*, 81:425–455, Dec 1994.
- [14] Heinz Werner Engl, Martin Hanke, and Andreas Neubauer. *Regularization of inverse problems*, volume 375. Springer Science & Business Media, 1996.
- [15] M. Figueiredo and R. Nowak. An EM Algorithm for Wavelet-Based Image Restoration. *IEEE Trans. Image Proc.*, 12(8):906–916, 2003.
- [16] Simon Foucart and Holger Rauhut. *A mathematical introduction to compressive sensing*, volume 1. Birkhäuser Basel, 2013.

- [17] Stephane Mallat. *A wavelet tour of signal processing: the sparse way*. Academic press, 2008.
- [18] D. Mumford and J. Shah. Optimal approximation by piecewise smooth functions and associated variational problems. *Commun. on Pure and Appl. Math.*, 42:577–685, 1989.
- [19] Neal Parikh, Stephen Boyd, et al. Proximal algorithms. *Foundations and Trends® in Optimization*, 1(3):127–239, 2014.
- [20] Gabriel Peyré. *L’algèbre discrète de la transformée de Fourier*. Ellipses, 2004.
- [21] J. Portilla, V. Strela, M.J. Wainwright, and Simoncelli E.P. Image denoising using scale mixtures of Gaussians in the wavelet domain. *IEEE Trans. Image Proc.*, 12(11):1338–1351, November 2003.
- [22] L. I. Rudin, S. Osher, and E. Fatemi. Nonlinear total variation based noise removal algorithms. *Phys. D*, 60(1-4):259–268, 1992.
- [23] Otmar Scherzer, Markus Grasmair, Harald Grossauer, Markus Haltmeier, Frank Lenzen, and L Sirovich. *Variational methods in imaging*. Springer, 2009.
- [24] C. E. Shannon. A mathematical theory of communication. *The Bell System Technical Journal*, 27(3):379–423, 1948.
- [25] Jean-Luc Starck, Fionn Murtagh, and Jalal Fadili. *Sparse image and signal processing: Wavelets and related geometric multiscale analysis*. Cambridge university press, 2015.